Miner Deposita (2018) 53:399–416
DOI 10.1007/s00126-017-0746-4

ARTICLE

Uranium-lead dating of hydrothermal zircon and monazite from the Sin Quyen Fe-Cu-REE-Au-(U) deposit, northwestern Vietnam

Xiao-Chun Li[1] · Mei-Fu Zhou[1] · Wei Terry Chen[2] · Xin-Fu Zhao[3] · MyDung Tran[4]

Received: 24 July 2016 / Accepted: 28 May 2017 / Published online: 28 June 2017

Abstract The Sin Quyen deposit in northwestern Vietnam contains economic concentrations of Cu, Au and LREE, and sub-economic concentration of U. In this deposit, massive and banded replacement ores are hosted in Neoproterozoic metapelite. The paragenetic sequence includes sodic alteration (stage I), calcic-potassic alteration and associated Fe-REE-(U) mineralization (stage II), Cu-Au mineralization (stage III), and sulfide-(quartz-carbonate) veins (stage IV). The Sin Quyen deposit experienced an extensive post-ore metamorphic overprint, which makes it difficult to precisely determine the mineralization age. In this study, zircon and monazite U-Pb geochronometers and the Rb-Sr isochron method are used to constrain the timing of mineralization. Zircon grains in the ore are closely intergrown or texturally associated with hydrothermal minerals of stage II (e.g., garnet, allanite, and hedenbergite). They may contain primary fluid inclusions and display irregular zoning in cathodoluminescence (CL) images. Zircon grains are rich in U (688 to 2902 ppm) and poor in Th (0.2 to 2.9 ppm). Their $\delta^{18}O_{V\text{-}SMOW}$ values range from 11.9 to 14.0‰, higher than those of typical magmatic zircon. These textural and compositional features imply that zircon precipitated from ^{18}O- and U-rich hydrothermal fluids, coeval with the minerals of stage II. Monazite occurs in close association with stage II magnetite and allanite and has low contents of Th (<2700 ppm), indicative of a hydrothermal origin. Hydrothermal zircon and monazite have indistinguishable U-Pb ages of 841 ± 12 and 836 ± 18 Ma, respectively, representing the timing of Fe-REE mineralization. There is no direct isotopic constraint on the timing of the Cu-Au mineralization, but geological observations suggest that the Cu-Au and Fe-REE ores most likely formed within a single evolved hydrothermal process. In the plot of $^{87}Rb/^{86}Sr$ vs. $^{87}Sr/^{86}Sr$, the composition of bulk-ore and biotite separates from ore lie along a reference line for 30 Ma, which is consistent with the timing of metamorphism in the region. The mineralization age of the Sin Quyen deposit falls within the overall age range (740 to 860 Ma) of the regional Neoproterozoic igneous rocks. This temporal linkage, in combination with the magmatic-like sulfur isotopes of sulfide minerals ($\delta^{34}S_{V\text{-}CDT}$ = −0.8 to 3.1), indicates that the mineralization may have a close genetic association with the Neoproterozoic igneous activity.

Editorial handling: R. Romer

Electronic supplementary material The online version of this article (doi:10.1007/s00126-017-0746-4) contains supplementary material, which is available to authorized users.

✉ Mei-Fu Zhou
mfzhou@hku.hk

[1] Department of Earth Sciences, The University of Hong Kong, Hong Kong, SAR, China

[2] State Key Laboratory of Ore Deposit Geochemistry, Institute of Geochemistry, Chinese Academy of Sciences, Guiyang 550081, China

[3] State Key Laboratory of Geological Processes and Mineral Resources, and Faculty of Earth Resources, China University of Geosciences, Wuhan 430074, China

[4] General Department of Geology and Minerals of Vietnam, Hanoi, Vietnam

Introduction

Determination of the timing of mineralization is a fundamental step in understanding ore genesis and regional

metallogeny, and thus is important for the identification of the most favorable geologic environments for undiscovered deposits. However, the age of iron oxide-copper-gold (IOCG) deposits may be difficult to determine. Many Precambrian IOCG deposits have experienced post-ore metasomatic and/or metamorphic events (Duncan et al. 2011; Ciobanu et al. 2013; Zhou et al. 2014), during which isotopic systems with relatively low closure temperatures may have been variably disturbed. Some IOCG deposits have endured several temporally discrete mineralization events (Chen et al. 2010; Zhao et al. 2013; Moreto et al. 2015a, b), which means that bulk-ore scale geochronological analyses may not be able to adequately distinguish such multiple hydrothermal events. Therefore, in order to obtain well-constrained mineralization ages, particularly for deposits formed in complex geological environments, it is necessary to analyze mineral phases at the microscale and to use radiogenic isotope systems that have high closure temperatures. It is well established that zircon and monazite can form from hydrothermal fluids (Schandl and Gorton 2004; Hoskin 2005; Schaltegger 2007; Deng et al. 2015). They are commonly resistant to metamorphic/hydrothermal modifications and contain high U and/or Th, but negligible common Pb (Chiaradia et al. 2013). Thus, hydrothermal zircon and monazite are ideal phases for determining mineralization ages. However, there are few studies using hydrothermal zircon and monazite U-Pb geochronology to date IOCG deposits (Valley et al. 2009; Conor et al. 2010; Jagodzinski 2014; Moreto et al. 2015b).

The Sin Quyen deposit is currently the major source of Cu in Vietnam, with annual production of 30,000 t Cu metal (Pham 2015a). Previous studies have focused on the geology, alteration, and mineralization styles of the Sin Quyen deposit and have recognized it as a typical IOCG deposit (McLean 2001). This deposit has a complex deformation and metamorphic history, making it difficult to determine the timing of the mineralization events. The lack of precise mineralization ages has hindered the understanding of the ore genesis. In this study, we present textures and compositions of zircon and monazite from the Sin Quyen deposit and demonstrate that they are hydrothermal in origin. In situ U-Pb dating of hydrothermal zircon and monazite from ore, and of magmatic zircon from a post-ore granitic dike places constraints on the timing of the mineralization. Because the Rb-Sr isotopic system can be easily disturbed during recrystallization (Chiaradia et al. 2013), whole-rock Rb-Sr isotopic data were also obtained to investigate their response to post-ore modification events. The dataset presented herein provides age constraints on the mineralization and modification history of the Sin Quyen deposit, and hence a better understanding of the ore genesis.

Regional geology

Northwestern Vietnam is bounded by the Red River fault to the north, and the Song Ma suture belt to the south (Fig. 1a). A Cenozoic tectonic event, the activation of the left-lateral, Ailao Shan-Red River (ASRR) shear zone as a response to the Cenozoic India-Eurasia collision, was influential in the region. Activation of the ASRR shear zone is assumed to have led to a large-scale southeastward displacement of the Indochina peninsula relative to South China (Tapponnier et al. 1990; Leloup et al. 1995).

The ASRR shear zone consists of four narrow metamorphic belts, namely, from northwest to southeast, Xuelong Shan, Diancang Shan, Ailao Shan-Phan Si Pan, and Day Nui Con Voi (Fig. 1a). The longest one, the Ailao Shan-Phan Si Pan belt, extends from the Yunnan province of China to northwestern Vietnam. The Sin Quyen deposit is hosted in the Phan Si Pan belt of northwestern Vietnam.

In the Phan Si Pan belt, a high-grade metamorphic complex is widely distributed, which includes the Suoi Chieng and Sin Quyen formations (Figs. 1b and 2). The Suoi Chieng Formation is mainly composed of granitic gneiss, biotite schist, biotite-amphibole gneiss, and amphibolite (Tran 2011a). The protoliths of these rocks include granitoids (~2.8 to ~2.2 Ga), terrigenous sediments, and mafic volcanic rocks. They were metamorphosed to amphibolite facies during at least two periods of metamorphism at 1.97 to 1.95 Ga, and 1.83 Ga (Pham 2015b; Wang et al. 2016). The Suoi Chieng Formation is conformably overlain by the Sin Quyen Formation (Fig. 2), which consists mainly of a lower unit of graphite schist and an upper unit of mica schist and gneiss (McLean 2001). The original lithologies of the Sin Quyen Formation include Paleoproterozoic to Neoproterozoic terrigenous sediments interbeded with minor carbonate and mafic volcanic rocks (Tran 2011b). The rocks were metamorphosed to the amphibolite facies. The major metamorphic event occurred during the Cenozoic (Liu et al. 2013), but a Late Permian to Early Triassic metamorphic event (~250 Ma) has also been locally identified (Pham 2010; Liu et al. 2013). The Upper Sin Quyen Formation is in fault contact with metasedimentary rocks of the Cambrian Cam Dung Formation at the surface (Fig. 2), and limestone and marble of the upper Proterozoic/Cambrian Sa Pa Suite at depth.

Abundant Neoproterozoic igneous rocks (751 to 843 Ma) intrude the metamorphic complex of the Phan Si Pan belt and its northwestward extension, the Ailao Shan belt in South China (Liu et al. 2008a; Pham et al. 2009; Qi et al. 2012, 2014; Cai et al. 2014, 2015; Li et al. 2017; Fig. 1). Many workers emphasize the arc-like signatures of the Neoproterozoic igneous rocks in the Ailao Shan-Phan Si Pan belt and propose that they were formed in a subduction-related setting (Qi et al. 2012, 2014; Cai et al. 2014, 2015; Li

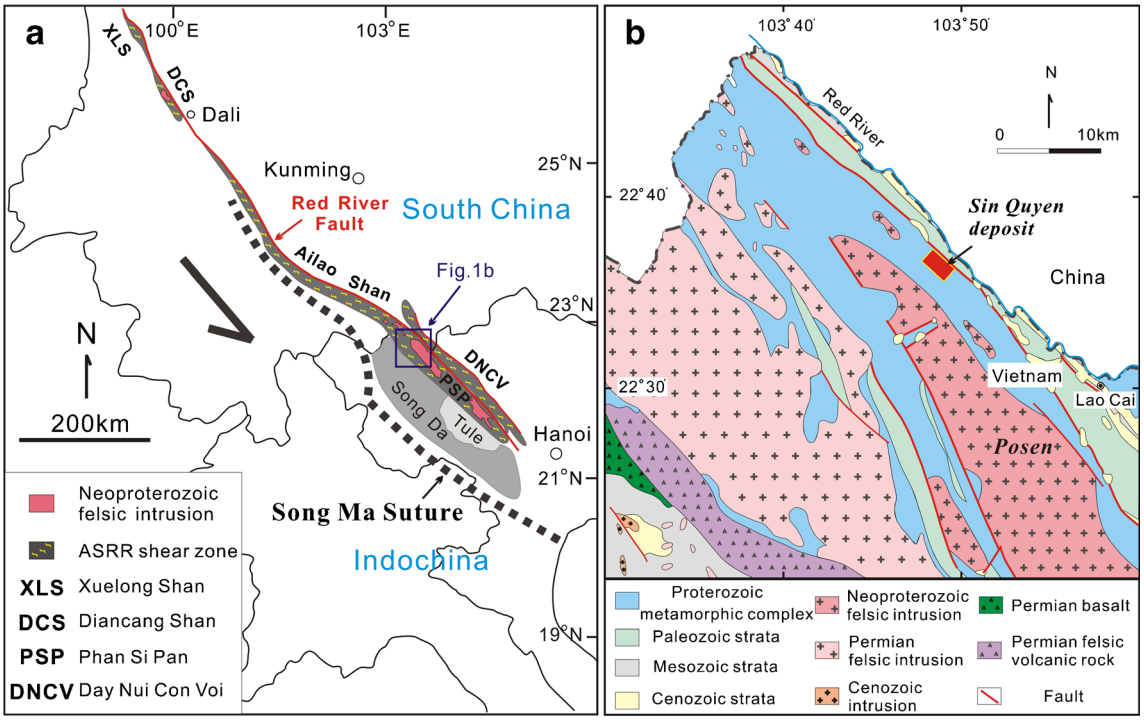

Fig. 1 **a** Simplified geotectonic map of northwestern Vietnam and southwestern China, showing the location of major tectonic units and highlighting the distribution of Neoproterozoic igneous rocks. *ASRR* Ailao Shan-Red River. **b** Geological map of the Sin Quyen region (modified from Bui (2005))

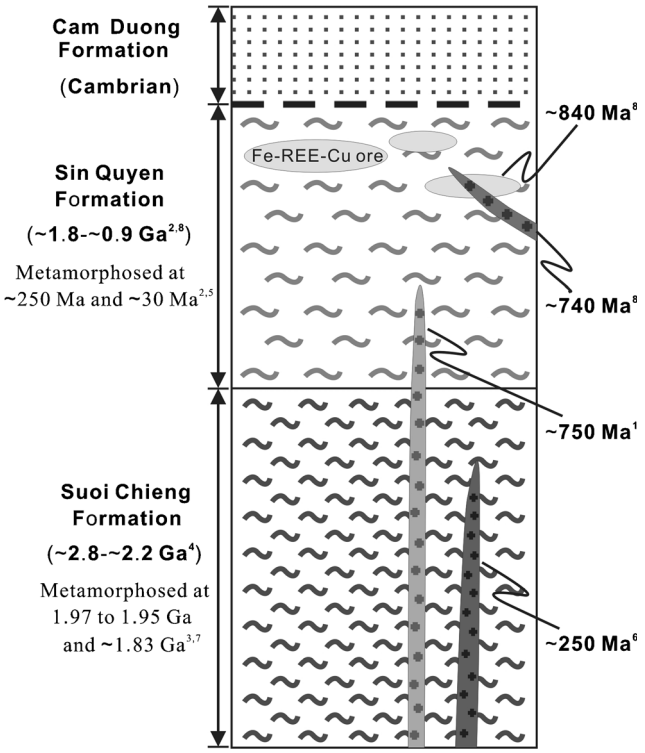

Fig. 2 Schematic illustration of rock relations in the Sin Quyen region. Data source: *1*, Pham et al. (2009); *2*, Pham (2010, 2015b); *3*, *4*, Tran (2011a); *5*, Liu et al. (2013); *6*, Usuki et al. (2015); *7*, Wang et al. (2016); *8*, this study

et al. 2017). Late Permian to early Triassic (249 to 259 Ma) alkaline to sub-alkaline granitoids occur in the northwestern part of the Phan Si Pan belt (Fig. 1b). These intrusions were genetically related to a mantle plume activity (Usuki et al. 2015). Rocks in the Phan Si Pan belt have been affected by deformation related to the Cenozoic left-lateral strike-slip shearing. They commonly show a schistosity trending NW-SE and dipping toward the northeast.

Several Fe-(Cu) deposits or prospects, including Sin Quyen, Nam Mit, Nam Chac, Suoi Thau, Pin Ngan Chai, and Lung Thang, are distributed along the Phan Si Pan belt (McLean 2001). The Sin Quyen deposit is the largest one, whereas the others are relatively small and of low grades.

Deposit geology

The Sin Quyen deposit is located ~1 km from the bank of the Red River, which marks the boundary between Vietnam and China in that area (Fig. 1b). Exploration in the 1990s showed that the Sin Quyen deposit contains 52.8 Mt ore at 0.91 wt.% Cu, 0.7 wt.% LREE (La, Ce, Pr, and Nd), and 0.44 g/t Au (Mclean 2001). Drilling to depths of −350 m has outlined an additional ~90 Mt of ore with an average grade of 0.9 wt.% Cu (Pham 2015a).

The orebodies occur within an elongated, NW-SE trending zone, with a width of 150 to 300 m, a length of approximately 2.5 km and a vertical extent of less than 600 m (Fig. 3). Ore and ore-related metasomatites are hosted in the gneiss, mica schist, and locally marble of the upper Sin Quyen Formation (Fig. 4a). The gneiss is mainly composed of biotite, feldspar, and quartz, and the mica schist mainly contains biotite, muscovite, quartz, and feldspar. The ore-hosting rocks are strongly deformed with shallow-dipping lineation, mylonitic fabrics, and asymmetrical tails on feldspars indicating left-lateral shearing (Fig. 5a).

According to McLean (2001), amphibolites, which are mainly composed of hornblende (66%), plagioclase (19%), and biotite (6%), are abundant in the mining area and are the

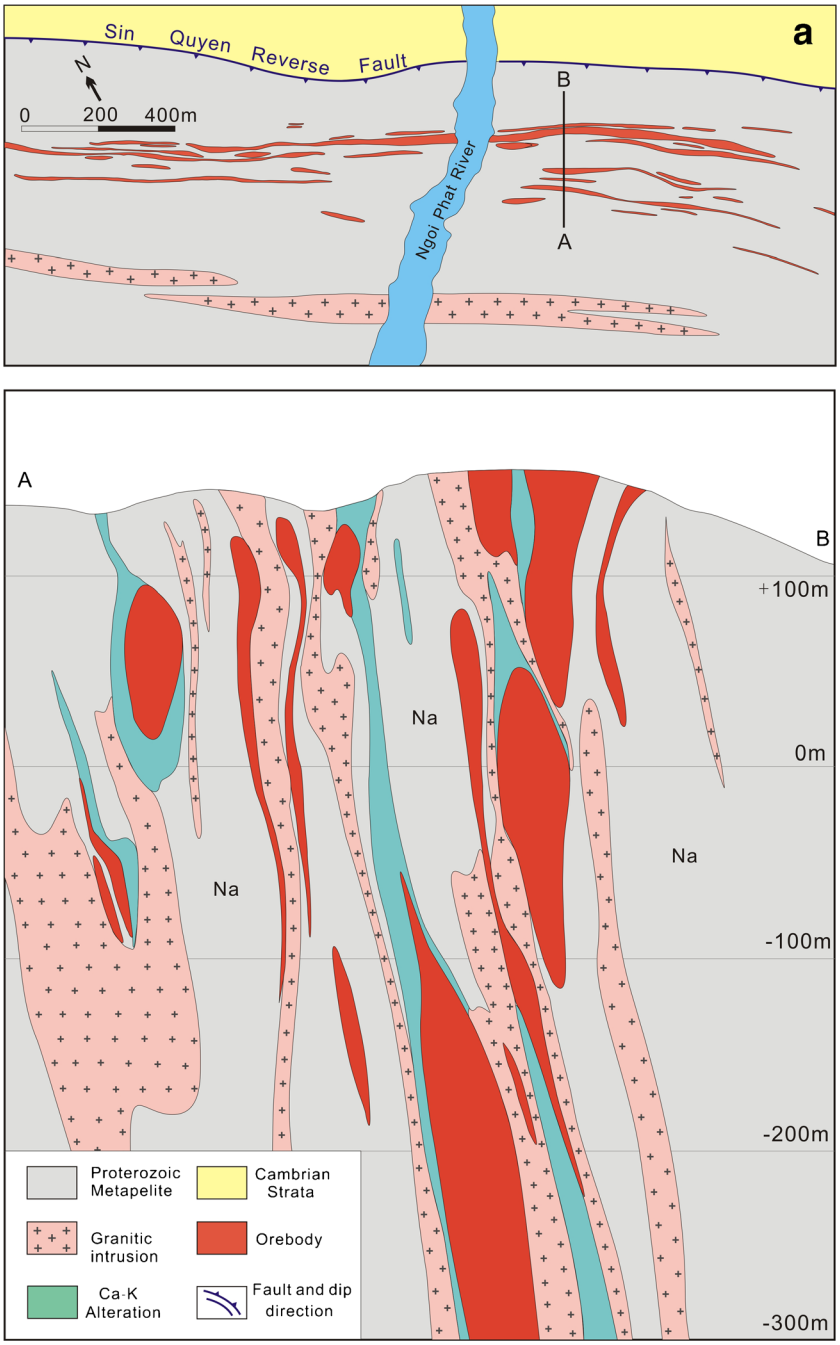

Fig. 3 **a** Simplified geological map of the Sin Quyen deposit (modified from Ta et al. (1975)). **b** Cross section A–B located in **a**, showing the shape and distribution of orebodies (modified from Mclean (2001)). Note that the amphibolite in Fig. 3 of Mclean (2001) is illustrated as Ca-K alteration halo in this figure. See text for explanations

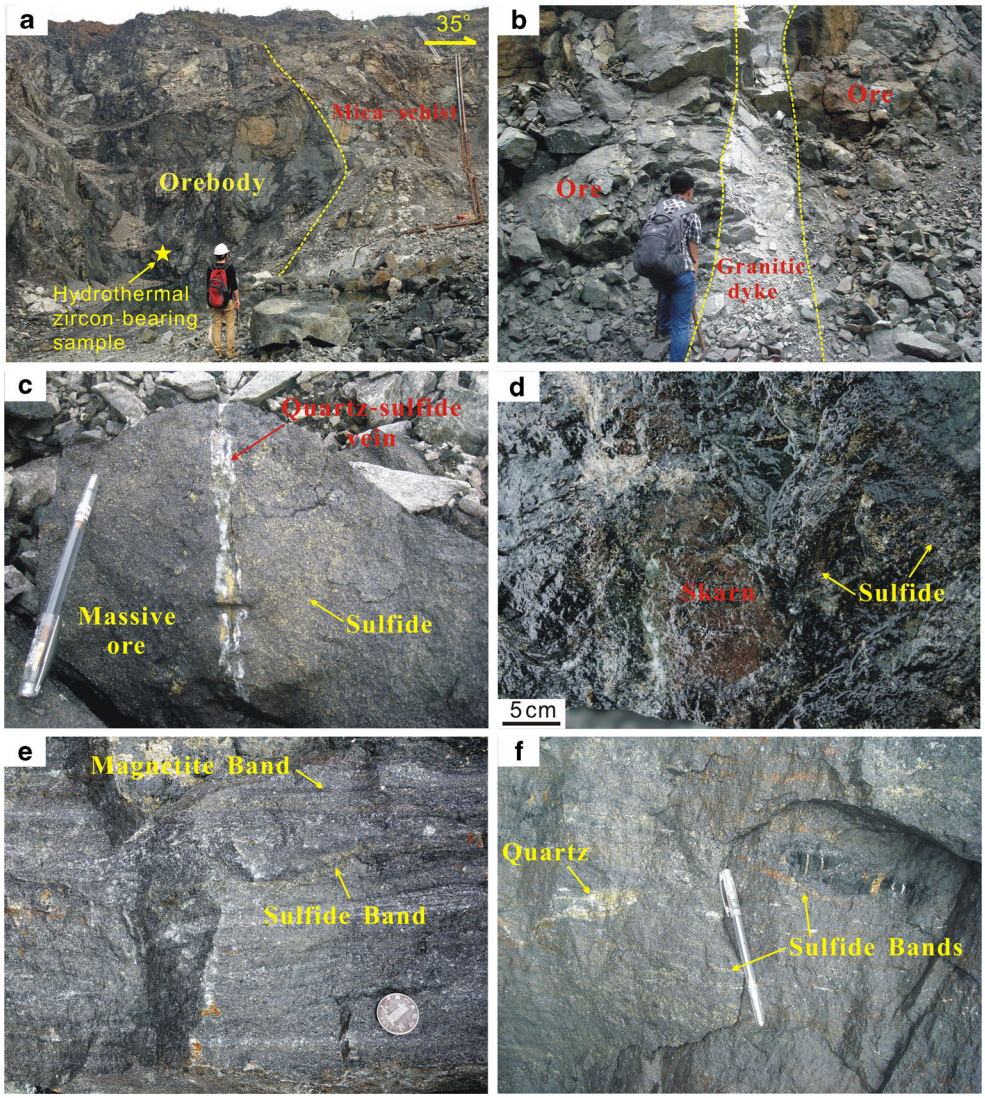

Fig. 4 **a** A large lenticular orebody hosted in mica-schist. Also shown is the location of the hydrothermal zircon-bearing sample. **b** Granitic dike intruding the orebody, characterized by strong fragmentation. **c** Massive ore sample that contains disseminated sulfide minerals. An undeformed quartz-sulfide vein cuts through the massive ore sample. **d** Massive ore sample that contains skarn-like alteration. Note that skarn occurs as small irregular body with gradual contact with host rock. **e** Banded ore sample that contains magnetite-rich and sulfide-rich bands. **f** Sulfide (+quartz) bands in a banded ore sample

main host for the ores (Fig. 5b). Our studies show that the amphibole and biotite from the amphibolites have compositions rather similar to hydrothermal amphibole and biotite from the ores, respectively. In addition, plagioclase in amphibolites has near end-member albite compositions (Na/(Na + Ca) > 0.9). Such Na-rich plagioclase is very uncommon in amphibolites of metamorphic in origin. Therefore, we propose that the "amphibolites" are essentially ore-related "metasomatites," rather than metamorphosed, mafic igneous rocks. Indeed, there are some small amphibolite bodies in the mining area, but they do not show any spatial association with orebodies. Apart from amphibolites, abundant granitic dikes/stocks also occur in the mining area (Fig. 3b). The granitic dikes/stocks have been variably deformed. It was assumed that the highly deformed dikes/stocks formed during the Proterozoic, whereas the slightly deformed ones were Permian (McLean 2001). However, recent dating shows that both the highly deformed and slightly deformed dikes/stocks were formed at Neoproterozoic (736 to 758 Ma) (Li et al. 2017). Field observations show that most granitic dikes/stocks are not mineralized, and thus postdated the mineralization (Fig. 4b). It is notable that some deformed granitic dikes/stocks, termed "granite-gneiss" by McLean (2001), are mainly composed of albite, biotite, and quartz, without K-feldspar (Fig. 5c). They are probably "metasomatites" that have experienced intensive albite

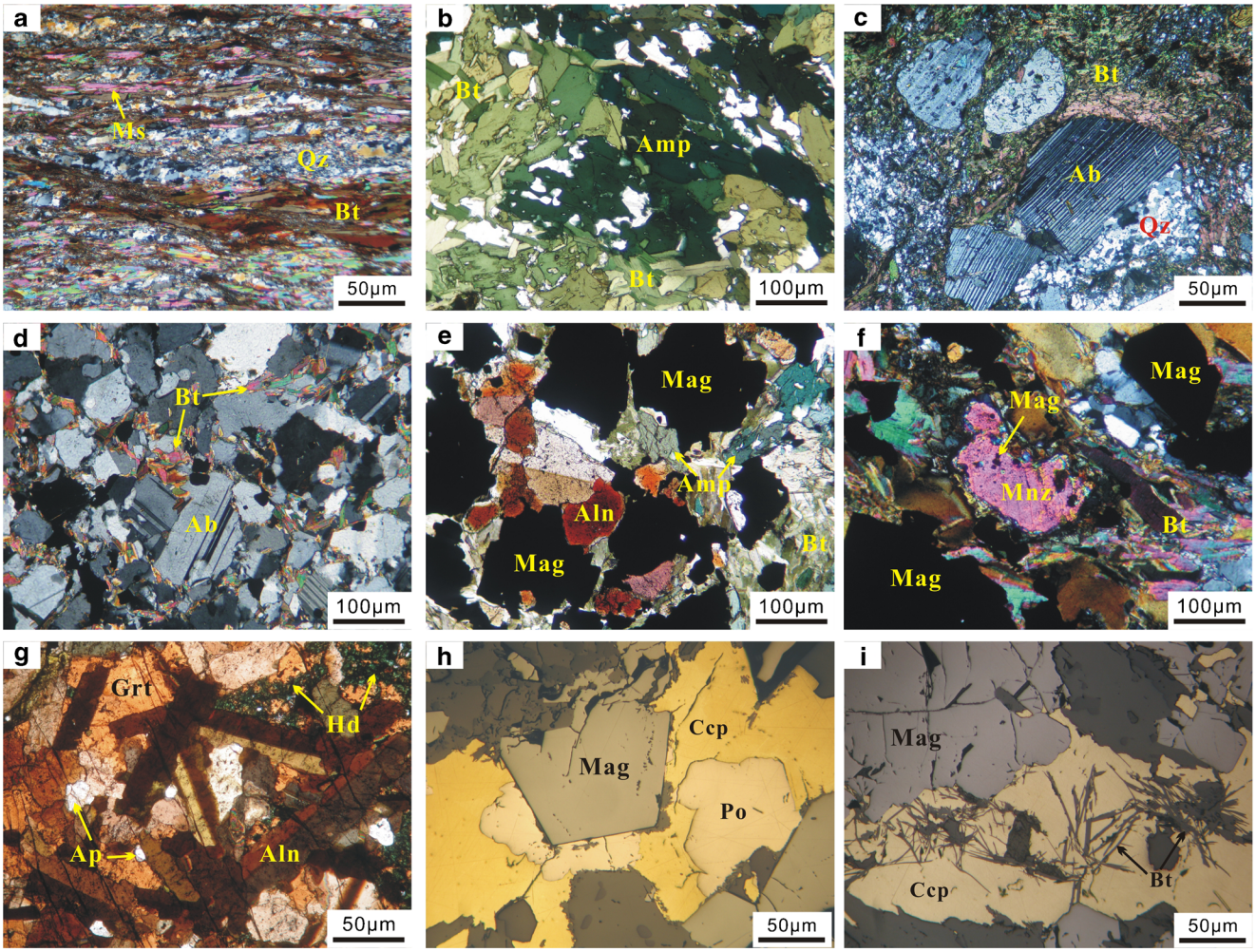

Fig. 5 **a** Ore-hosting schist, which contains mainly biotite, muscovite and quartz. **b** Amphibolite described by Mclean (2001). **c** Granite-gneiss described by Mclean (2001). **d** Pre-ore albite grains in sodic altered rocks. **e** Typical mineral assemblage of stage II (magnetite + allanite + amphibole + biotite). **f** Typical mineral assemblage of stage II (magnetite + monazite + biotite). **g** Typical mineral assemblage of skarn-like rocks (grossularitic-andraditic garnet + allanite + hedenbergite). **h** Magnetite of stage II is surrounded by pyrrhotite and chalcopyrite of stage III. **i** Biotite is intergrown with chalcopyrite of stage III. *Ab* albite, *Aln* allanite, *Amp* amphibole, *Ap* fluorapatite, *Bt* biotite, *Ccp* chalcopyrite, *Grt* garnet, *Hd* hedenbergite, *Mag* magnetite, *Mnz* monazite, *Ms* muscovite, *Po* pyrrhotite, *Qz* quartz

alteration and later-stage biotite alteration, rather than magmatic intrusions.

A number of northwest-trending faults in the upper Sin Quyen Formation are generally parallel to, and interpreted to represent splays of the major Red River Fault. These faults confine a series of steeply dipping, discontinuous "broken zones," which enclose rocks that have been variably fractured, sheared, and dislocated. The economic mineralization is mainly concentrated in these "broken zones" (McLean 2001). Orebodies are mostly lenticular in shape, extending NW-SE and dipping steeply to the northeast (Fig. 3). The orebodies consist mainly of massive or banded replacement ores (Fig. 4c–f), with minor vein-type varieties. Iron, Cu, and REE commonly coexist in the ores, but their proportions are spatially variable.

On the basis of macro- and microtextural relationships, four principal stages of alteration and mineralization can be identified in the Sin Quyen deposit: pre-ore sodic alteration (I), calcic-potassic alteration and associated Fe-REE-(U) mineralization (II), Cu-Au mineralization (III), and sulfide-(quartz-carbonate) veins (IV). Such a sequence is generally comparable with that of McLean (2001). The pre-ore sodic alteration typically involves replacement of the ore-hosting rocks by albite-rich plagioclase. It affected rocks almost throughout the whole deposit. The rocks in the vicinity of the orebodies were commonly altered to "albitite" (Fig. 5d). The extensive sodic alteration was followed by more localized and intensive calcic-potassic alteration (amphibole + biotite ± hedenbergite ± fluorapatite ± titanite) and associated Fe-REE-(U) mineralization (magnetite + allanite ± monazite ±

bastnaesite ± uraninite) (Fig. 5e, f). Magnetite, allanite, and associated gangue minerals are not deformed in massive ores (Fig. 4c), but they are commonly aligned along foliation in banded ores (Fig. 4e, f). In places, rocks show skarn-like calc-silicate alteration, consisting mainly of grossularitic-andraditic garnet, hedenbergite, allanite, and sulfide minerals (Figs. 4d and 5g). They are generally present as small, irregular bodies which are transitional to their surroundings. In the skarn-like rocks, allanite is intergrown with garnet and euhedral magnetite is enclosed by hedenbergite. These textural observations suggest that the skarn-like alteration was synchronous with the Fe-REE mineralization. Stage III Cu-Au mineralization is confined mainly within the Fe-REE mineralization zones, and to a much lesser extent in the meta-sedimentary rocks of the upper Sin Quyen Formation. It is characterized by abundant sulfide minerals, mainly chalcopyrite and pyrrhotite, which occur as disseminations, bands, massive accumulations, or veins overprinting the minerals of stages I and II (Fig. 5h, i). The sulfide minerals show weak/no deformation in massive ores (Fig. 4c, d). However, they are commonly confined to or oriented along the foliation in banded ores (Fig. 4e, f). This is different from McLean's observation, which showed that the main-stage sulfide minerals are rarely deformed (McLean 2001). Biotite and quartz may occur in association with sulfide minerals (Figs. 4f and 5i). In stage IV, sulfide-(quartz-carbonate) veins with varying widths (<1 to >10 cm) develop crosscutting the Fe-Cu-REE ore, ore-hosting meta-sedimentary rocks, and granitic intrusions (Fig. 4c). Sulfide minerals of this stage are locally abundant, but overall, they host insignificant ore resources. They are mostly undeformed, and their formation seems to be related to the remobilization of pre-existed sulfide minerals. It is notable that some deformed quartz-sulfide veins were documented by McLean (2001), which are earlier than the main-stage sulfide minerals. Such type of veins was rarely encountered in our observations.

Mineralogy of zircon and monazite

Zircon from ore sample

The zircon-bearing ore sample (SQ152) was collected in the middle part of a large orebody in the eastern mining area (Fig. 4a). This sample consists of garnet (60 vol.%), allanite (15 vol.%), hedenbergite (10 vol.%), amphibole (5 vol.%), sulfide minerals (5 vol.%), and minor amounts of magnetite, fluorapatite, and titanite. Garnet, allanite, and hedenbergite formed earlier than amphibole. Sulfide minerals formed during the latest phase overprinting all other minerals.

Zircon grains occur as either irregular aggregates surrounding garnet (Fig. 6a), or euhedral to subhedral single grains in contact with garnet, hedenbergite, titanite, or allanite (Fig. 6b, c). Zircon grains are pale brown or colorless and usually show murky or dirty appearance in transmitted light (Fig. 6d–f). They have prismatic to irregular crystal shapes, with lengths ranging from 50 to 150 μm (mostly 80 to 100 μm). Zircon grains usually contain some mineral inclusions, mainly garnet (Fig. 6g). The inclusions appear to have been trapped at the time of zircon growth, with no evidence for later precipitation along fractures. Zircon grains may also contain fluid inclusions, which are typically small (<5 μm) and have rounded to negative crystal shapes (Fig. 6d–f). Most fluid inclusions are two-phase (liquid + vapor) aqueous inclusions. Three-phase inclusions, composed of a solid phase, a vapor bubble, and a daughter mineral, are rare. The fluid inclusions are commonly scattered in zircon, rather than distributed along healed microfractures (Fig. 6d–f). Thus, they are interpreted to be trapped during zircon crystallization (primary inclusions).

In CL images, zircon grains from the ore sample have complex internal textures and can be classified into four types (Fig. 6h). Type A grains are subordinate and have high-luminescence cores with oscillatory zoning, discordantly surrounded by low-luminescence rims. Type B grains have well-developed oscillatory zoning, which may be overgrown by a very thin, continuous or discontinuous, high-luminescence margin. Type C grains have oscillatory-zoned domains irregularly overprinted by domains with patchy or cloudy zoning. Type D grains are relatively abundant and comprise irregularly distributed domains with patchy, cloudy, or flow zoning (for simplicity, they are together termed as "irregular" zoning).

Monazite from ore sample

The monazite-bearing ore sample (LC44) was collected from a relatively small orebody in the western mining area. This orebody is hosted by mica schist and has been intruded by several deformed granitic dikes. The sample is composed of albite (10 vol.%), magnetite (20 vol.%), allanite (15 vol.%), amphibole (20 vol.%), sulfide minerals (15 vol.%), and biotite (15 vol.%). Albite is the earliest phase (stage I) (Fig. 5d), followed by magnetite, allanite, amphibole, and biotite (stage II) (Fig. 5f), and then sulfide minerals (stage III).

Monazite is heterogeneously distributed in this sample, and locally its volume proportion can reach 10%. Monazite is large in size (100 to 500 μm) and euhedral to subhedral in shape (Figs. 5f and 7). Under BSE imaging, monazite grains are homogeneous. They may contain some irregularly distributed pore-bearing domains (Fig. 7). Euhedral to subhedral magnetite and allanite commonly occur as inclusions in monazite (Figs. 5f and 7). Some monazite grains are surrounded by allanite and fluorapatite.

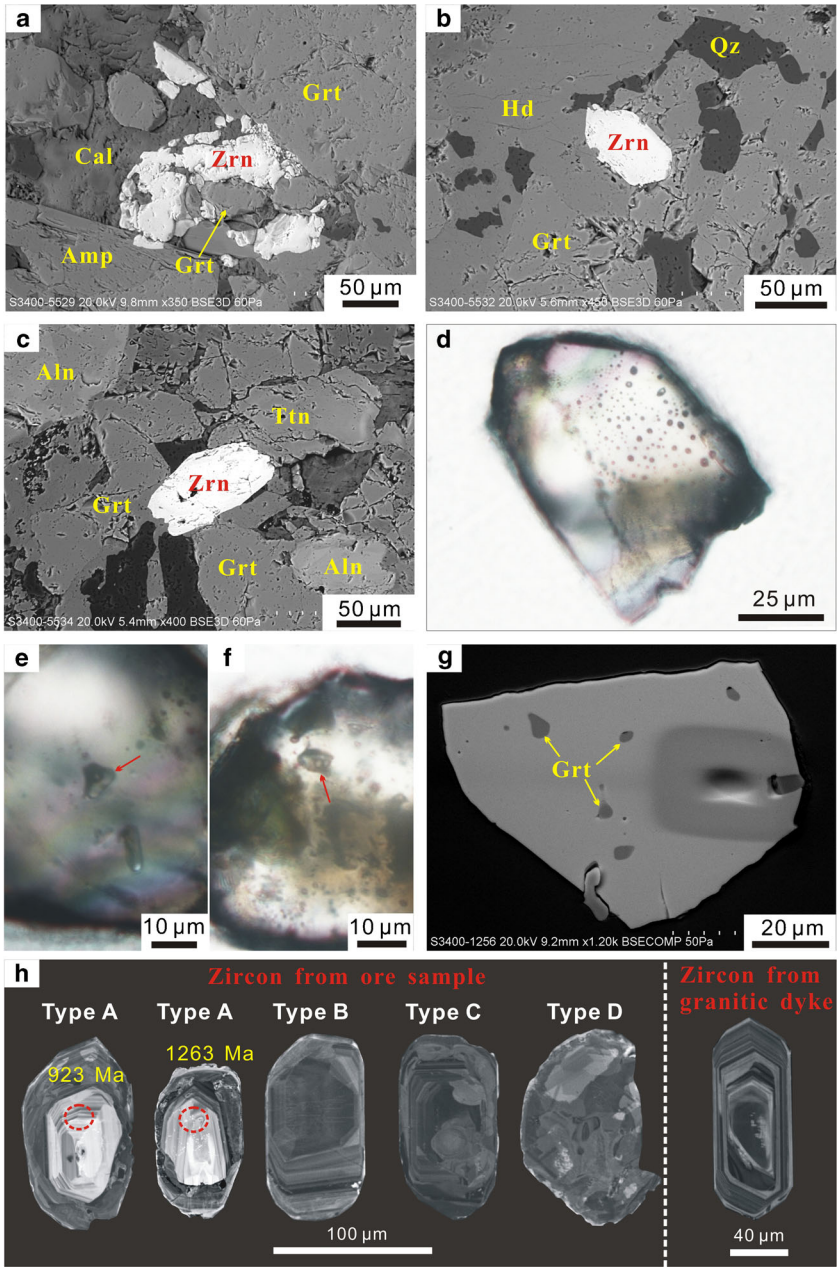

Fig. 6 **a** Zircon aggregates in close association with garnet. **b** Euhedral zircon in contact with hedenbergite and garnet. **c** Subhedral zircon in contact with garnet and titanite. **d** Zircon containing abundant fluid inclusions. **e** A typical two-phase fluid inclusion (marked by *red arrow*) in zircon. **f** A typical three-phase fluid inclusion (marked by *arrow*) in zircon. **g** Zircon containing several garnet inclusions. The *rectangle pit in the right* is caused by sputtering of the zircon during SIMS analysis. **h** CL images of zircon grains. Type A zircon grains have a high-luminescence core but a low-luminescence rim. Type B grain has prismatic morphology and well-developed oscillatory zoning. Type C grain has oscillatory-zoned regions overprinted by irregularly zoned regions. Type D grain shows irregular zoning. Zircon from post-ore granitic dike shows typical oscillatory zoning. The U-Pb analyses pits and $^{207}Pb/^{206}Pb$ ages of the high-luminescence cores in type A zircon are shown. *Cal* calcite, *Zrn* zircon. Other abbreviations as in Fig. 5

Zircon from post-ore granitic dike

Zircon grains from a deformed post-ore granitic dike are pale brown to colorless and are characterized by long prismatic morphology. The lengths of these grains range from 50 to 150 μm, with length/width rations of 2:1 to 4:1. In CL images, most grains show well-developed oscillatory zoning (Fig. 6h), consistent with a magmatic origin (Hoskin and Schaltegger 2003). Minor amounts of grains show patched zoning or cloudy zoning, which is indicative of hydrothermal overprint.

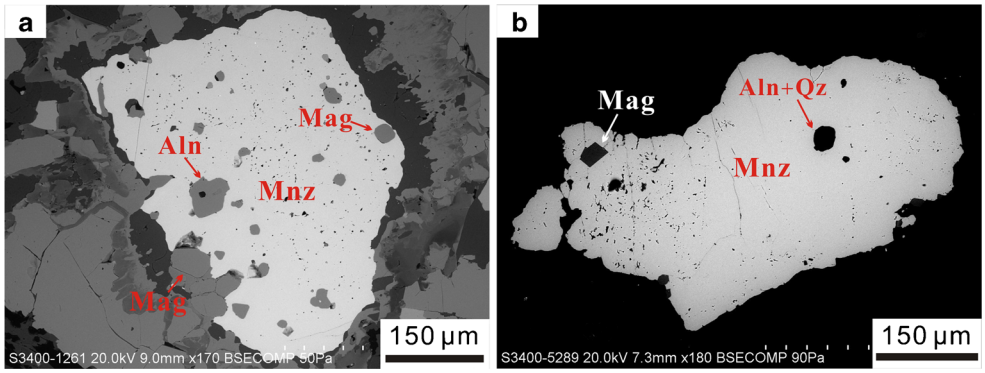

Fig. 7 **a** BSE image of a monazite grain, which contains several magnetite and allanite inclusions. **b** BSE image of a monazite grain, which contains inclusions of magnetite, allanite, and quartz. Note that some regions in the two monazite grains contain many pores

Analytical methods

Mineral trace element analysis

Trace elements of zircon were analyzed by LA-ICP-MS at the State Key Laboratory of Geological Processes and Mineral Resources, China University of Geosciences, Wuhan. Laser sampling was performed using a GeoLas 2005 system with wavelength of 193 nm. An Agilent 7500a ICP-MS was used to acquire ion-signal intensities. Analyses were performed with a beam diameter of 44 μm and a repetition rate of 6 Hz. Helium was applied as a carrier gas. Argon was used as the make-up gas and mixed with the carrier gas via a T-connector before entering the ICP. Each analysis incorporated a background acquisition of ~25-s (gas blank) followed by ~50-s data acquisition from the sample. Standard NIST 612 was used as an external calibration standard, which was analyzed twice after every eight sample analyses. Silicon was used as the internal standard. Precision based on repeated analysis of standard is better than 10%.

Trace elements of allanite, monazite, and garnet were analyzed using a RESOlution M-50 laser ablation system with wavelength of 193 nm coupled to an Agilent 7500a type ICP-MS at the Guangzhou Institute of Geochemistry, Chinese Academy of Sciences. Analyses were performed with a beam diameter of 32 μm and a repetition rate of 4 Hz. Helium was used as a carrier gas to enhance the transport efficiency of the ablated material. The counting times were ~25 and ~40 s for the background and sample analyses, respectively. Standard NIST 610 was used as an external calibration standard, which was analyzed twice after every eight sample analyses. Calcium was used as the internal standard for allanite and garnet, and Ce for monazite. Precision based on repeated analysis of standards is better than 10%. Data reduction was performed by the software ICPMSDataCal (Liu et al. 2008b). Trace element data are available in Electronic Supplementary Material (ESM)-Table 1.

Zircon U-Pb dating

Zircon crystals were separated from crushed samples using conventional density and magnetic separation techniques. The separated zircon grains were then mounted in epoxy resin, and the mounts were ground and polished to section the crystals in half for analyses. Prior to U-Pb isotopic analyses, zircon was examined with transmitted and reflected light and further with CL images to reveal their internal textures.

The U-Pb dating of zircon from the ore sample was conducted using a Cameca IMS-1280 Secondary Ion Mass Spectrometer (SIMS) at the Institute of Geology and Geophysics, Chinese Academy of Sciences (IGGCAS). Analytical procedures are similar to those reported by Li et al. (2009). The primary O_2^- ion beam spot is about 20 × 30 μm in size. Positive secondary ions were extracted with a 10-kV potential. In the secondary ion beam optics, a 60-eV energy window was used, together with a mass resolution of ca. 5400 (at 10% peak height), to separate Pb^+ peaks from isobaric interferences. A single electron multiplier was used in ion-counting mode to measure secondary ion beam intensities by peak jumping mode. Pb/U calibration was performed relative to zircon standard TEMORA 2 ($^{206}Pb/^{238}U$ age = 417 Ma; Black et al. 2004); U and Th concentrations were calibrated against zircon standard 91500. Measured compositions were corrected for common Pb using non-radiogenic ^{204}Pb. Corrections are sufficiently small to be insensitive to the choice of common Pb composition, and an average of present-day crustal composition (SStacey and Kramers 1975) was used. Data reduction was carried out using the Isoplot/Ex v.2.49 program (Ludwig 2001). In order to monitor the external uncertainties of measurements, an in-house standard zircon Qinghu was analyzed. Six measurements on Qinghu zircon yielded a concordia age of 160 ± 2 Ma, which is in good agreement with the recommended U-Pb age of 159.5 ± 0.2 Ma (Li et al. 2009). Uranium-lead dating results are available in ESM-Table 2.

The U-Pb dating of zircon from the post-ore granitic dike was conducted by LA-ICP-MS at the State Key Laboratory of Geological Processes and Mineral Resources, China University of Geosciences, Wuhan. Detailed operating conditions are similar as described by Liu et al. (2008a). Laser sampling was performed using a GeoLas 2005 system with wavelength of 193 nm. An Agilent 7500a ICP-MS instrument was used to acquire ion-signal intensities. Helium was applied as a carrier gas. Argon was used as the make-up gas and mixed with the carrier gas via a T-connector before entering the ICP. Analyses were performed with a beam diameter of 44 μm and a repetition rate of 6 Hz. Each analysis incorporated a background acquisition of ~20 s followed by ~50-s data acquisition for the sample. Zircon 91500 was used as external standard for U-Pb dating. Data reduction was carried out using the software ICPMSDataCal. In order to monitor the external uncertainties of measurements, a zircon standard GJ-1 was analyzed. Five measurements yielded a weighted average $^{206}Pb/^{238}U$ age of 606 ± 4 Ma, in agreement with the recommended age of 608.5 ± 0.4 Ma (Jackson et al. 2004). Uranium-lead dating results are available in ESM-Table 3.

Oxygen isotope analysis of zircon

Oxygen isotope composition of zircon was measured using the CAMECA IMS-1280 SIMS at IGGCAS. The detailed analytical procedure was described by Li et al. (2010). The Cs^+ primary ion beam was accelerated at 10 kV, with an intensity of 2 nA corresponding to a beam size of 10 μm in diameter. A normal incidence electron flood gun was used to compensate for sample charging. Negative secondary ions were extracted with a −10-kV potential. Oxygen isotopes were measured using multicollection mode. Measured $^{18}O/^{16}O$ ratios were standardized to Vienna Standard Mean Ocean Water compositions (VSMOW, $^{18}O/^{16}O$ = 0.0020052), and then corrected for the instrumental mass fractionation factor (IMF). The IMF was obtained using the Durango fluorapatite as a reference with a $\delta^{18}O$ value of 9.4‰ (Trotter et al. 2008). The internal precision of a single analysis is generally better than 0.2‰ (2σ standard error) for $^{18}O/^{16}O$ ratio. The Qinghu zircon standard was measured to monitor the accuracy of the analytical procedure. Fourteen measurements of the Qinghu zircon yielded a weighted mean $\delta^{18}O$ value of 5.50 ± 0.11‰ (2σ), which is consistent, within uncertainties, with the reported value of 5.39 ± 0.22‰ (Li et al. 2013). Oxygen isotopic data are available in ESM-Table 4.

Monazite U-Pb dating

Monazite U-Pb dating was conducted using an Agilent ICP-MS, equipped with a Geolas 193-nm excimer laser ablation system at IGGCAS. The analytical procedure follows that described by Liu et al. (2012). The monazite grains were analyzed in thin sections. Before analysis, transmission and reflection photomicrographs and BSE images were used to examine inclusions, cracks, and zoning. Analyses were performed with a spot size of 32 μm and a repetition rate of 6 Hz. Helium was used as the carrier gas and mixed with argon prior to entering the ICP torch. Each spot analysis consists of approximately 20-s background acquisition and 45-s sample data acquisition. A matrix-matched external standard 44069 ($^{207}Pb/^{206}Pb$ = 0.05532, $^{207}Pb/^{235}U$ = 0.06811, and $^{206}Pb/^{238}U$ = 0.5195; Aleinikoff et al. 2006) was used to correct the U/Pb fractionation and the instrumental mass discrimination. The raw count of ^{204}Pb is near zero, so common Pb correction was not made. The data reduction was carried out using the software package GLITTER 4.0. The Namaqua-1 monazite was measured as an external standard to monitor the accuracy of the analytical procedure. Seven spots yielded a weighted mean $^{206}Pb/^{238}U$ age of 1051 ± 31 Ma (2σ), which is consistent, within uncertainties, with the reported value of 1047 ± 7 Ma (Liu et al. 2012). Uranium-lead dating results are available in ESM-Table 5.

Rb-Sr isotopic analysis

The Rb-Sr isotopic composition of bulk-ore and biotite separates were analyzed, following procedures described by Chu et al. (2009). About 100 mg of powder was weighed into 7 ml Savillex™ Teflon beakers, and appropriate amounts of mixed ^{87}Rb-^{84}Sr spikes were added. Samples were dissolved by HF + HNO_3 (with a ratio of 2:1). Rubidium and Sr were separated using standard ion-exchange resins. The Rb-Sr isotopic compositions were measured using an IsoProbe-T thermal ionization mass spectrometer (GV instruments, England), at IGGCAS. Measured $^{87}Sr/^{86}Sr$ ratio was corrected for mass fractionation using $^{86}Sr/^{88}Sr$ = 0.1194. During the period of data collection, the measured values for the NBS-987 Sr standard was $^{87}Sr/^{86}Sr$ = 0.710245 ± 12 (2σ). The USGS reference material BCR-2 was measured for Rb-Sr isotopic composition to monitor the accuracy of the analytical procedures, with the following results: 47.5 ppm Rb, 341.1 ppm Sr, $^{87}Sr/^{86}Sr$ = 0.705042 ± 9 (2σ). These values are comparable with the reported reference values (GeoREM, http://georem.mpch-mainz.gwdg.de/). Based on repeated analysis of standards and blanks, the total procedural blanks are <40 pg for Rb and <350 pg for Sr. Rubidium-strontium isotopic compositions are available in ESM-Table 6.

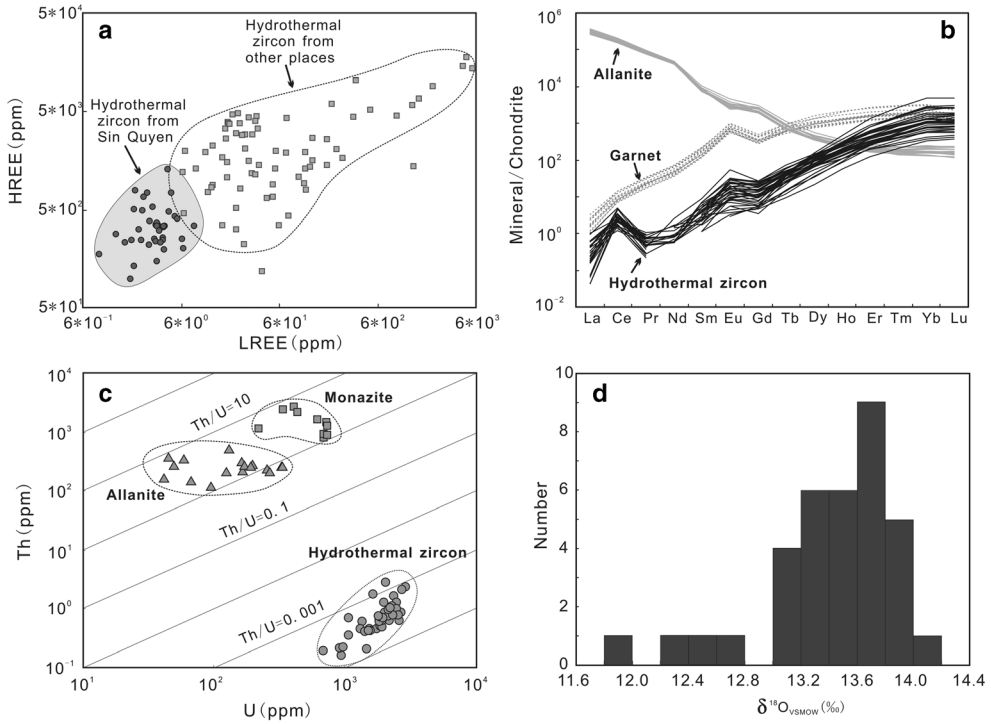

Fig. 8 **a** HREE vs. LREE diagram for hydrothermal zircon from the Sin Quyen deposit and from the Boggy Plain Zoned Pluton aplite, Australia (Hoskin 2005); Yankee Lodes and Paradise Lode, Mole Granite, Australia (Pettke et al. 2005); migmatitic granite, southwest Sweden (Rimsa et al. 2007); the Tamlalt-Menhouhou gold deposit, Morocco (Pelleter et al. 2007); the magnetite-apatite deposits in the Adirondack Highlands, USA (Valley et al. 2010); the Dexing porphyry copper deposit, China (Zhou et al. 2012); and the Dongping gold deposit, China (Bao et al. 2014). **b** Chondrite-normalized REE patterns for hydrothermal zircon, allanite, and garnet from the Sin Quyen deposit. **c** Th vs. U diagram for hydrothermal zircon, monazite, and allanite from the Sin Quyen deposit. **d** Histogram of the $\delta^{18}O_{V\text{-}SMOW}$ values of hydrothermal zircon from the Sin Quyen deposit

Sulfur isotopic analysis

Sulfide minerals from ore samples were chosen for in situ S isotope analysis. The analyses were performed in thin sections, using a Nu Plasma HR multicollector ICP-MS at the Geological Survey of Finland in Espoo together with a Photon Machine Analyte G2 laser microprobe. The main analytical procedure was described by Gilbert et al. (2014). Samples were ablated in He gas (gas flows = 0.4 and 0.1 l/min) within a HelEx ablation cell. During the ablation, the data were collected in static mode (^{32}S, ^{34}S). Pyrite and pyrrhotite were ablated at a spatial resolution of 50 μm at 5 Hz, using a fluence of 0.83 J/cm^2. Chalcopyrite was ablated at a spatial resolution of 50 μm at 8 or 10 Hz, using a fluence of 0.55 J/cm^2. Each spot consists of approximately 20-s background acquisition and 50- to 60-s sample data acquisition. Measured $^{32}S/^{34}S$ ratios were standardized to Vienna Canyon Diablo Troilite compositions (VCDT, $^{32}S/^{34}S$ = 22.6436). Two pyrite standards were used for external standard bracketing (PPP-1) and quality control (PY2), respectively. The in-house standard PY2 has been previously measured by gas source mass spectrometry. For a recommended $\delta^{34}S_{V\text{-}CDT}$(‰) value of −0.4 ± 0.5‰, we have obtained an average value of −0.2 ± 0.4‰ (n = 35). Two in-house chalcopyrite standards have been used for external standard bracketing (CPY1) and quality control (CPY2), respectively. The standard CPY2 has been previously measured by gas source mass spectrometry. For a recommended $\delta^{34}S_{V\text{-}CDT}$(‰) value of −0.7 ± 0.5‰, we have obtained an average value of −0.4 ± 0.4‰ (n = 18). Sulfur isotope data are available in ESM-Table 7.

Analytical results

Mineral composition

Zircon grains from the ore sample, except for high-luminescence cores in type A grains, contain low REE (103 to 1303 ppm), particularly LREE (La to Eu) (0.87 to 7.95 ppm; Fig. 8a). Their chondrite-normalized REE patterns have steep positive slope, with positive Ce anomalies and

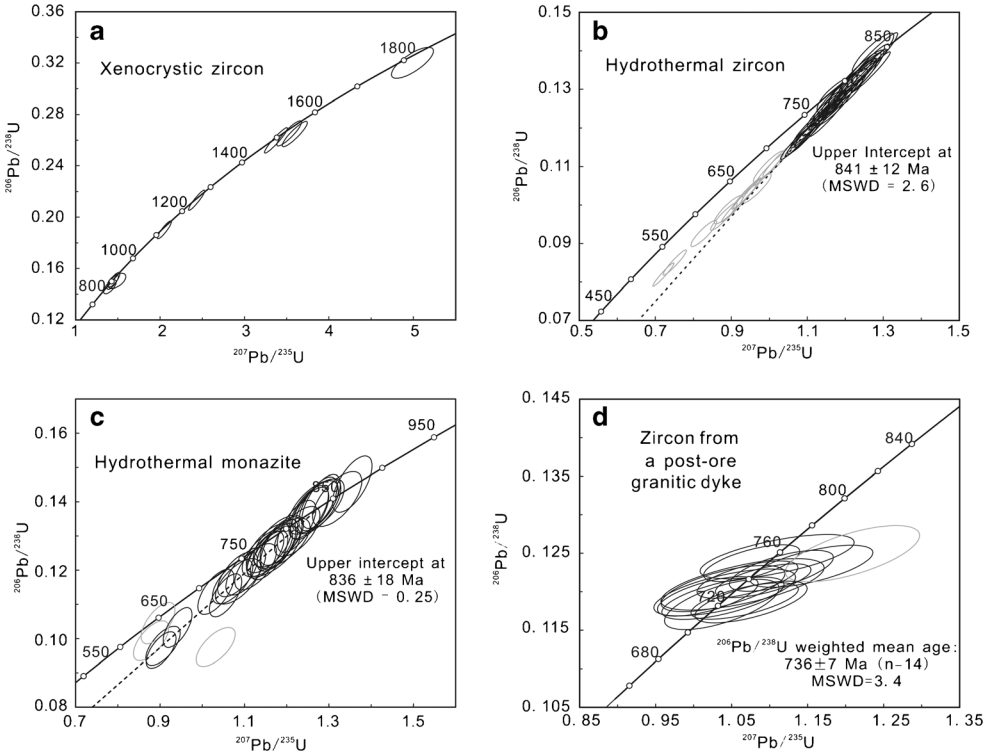

Fig. 9 **a** Concordia diagram showing SIMS U-Pb dating results for high-luminescence cores in type A zircon. **b** Concordia diagram showing SIMS U-Pb dating results for hydrothermal zircon. *Gray ellipses* were not included in the age calculation. **c** Concordia diagram showing LA-ICP-MS U-Pb dating results for monazite. *Gray ellipses* were disregarded in the age calculation. **d** Concordia diagram showing LA-ICP-MS U-Pb dating results for zircon from granitic dike. The *gray ellipse* was disregarded in the age calculation

positive (to slightly negative) Eu anomalies (Fig. 8b). They are rich in U (688 to 2902 ppm, by SIMS; 560 to 2270 ppm, by LA-ICP-MS), and very poor in Th (0.2 to 2.9 ppm, by SIMS; 0.1 to 1.4 ppm, by LA-ICP-MS; Fig. 8c). They have $\delta^{18}O_{V\text{-}SMOW}$ values ranging from 11.9 to 14.0‰ (Fig. 8d).

LA-ICP-MS analyses were conducted on both pore-free and pore-bearing domains of monazite. The two domains have very similar LREE contents, but the pore-free domains contain less HREE (Gd to Lu) and Y (2883 to 5121 ppm) than the pore-bearing domains (5755 to 10,739 ppm). The pore-free domains contain 804 to 2634 ppm Th and 222 to 737 ppm U. Compared with the pore-free domains, the pore-bearing domains generally contain lower Th (238 to 1473 ppm) and U (129 to 574 ppm).

Allanite crystals from ore samples are rich in LREE, with lower HREE. Thus, their chondrite-normalized REE patterns have steep negative slope ($(La/Yb)_N$ = 1155 to 2369) (Fig. 8b). Their Th and U concentrations range from 121 to 521 ppm and from 42 to 332 ppm, respectively.

Garnet crystals coexisting with zircon have high concentrations of HREE (815 to 1715) and Y (1490 to 3213 ppm), and relatively low concentrations of LREE (73 to 137 ppm). In the chondrite-normalized REE diagram, they have steep positive slope for the LREE ($(La/Eu)_N$ = 0.002 to 0.004) and shallow positive slope for the HREE ($(Gd/Lu)_N$ = 0.14 to

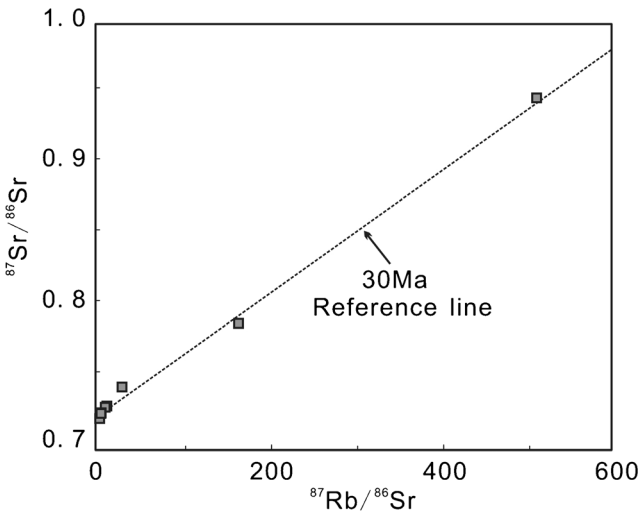

Fig. 10 $^{87}Rb/^{86}Sr$ vs. $^{87}Sr/^{86}Sr$ diagram for bulk ore and biotite separates from ores. A reference Rb-Sr isochron of 30 Ma is shown for comparison

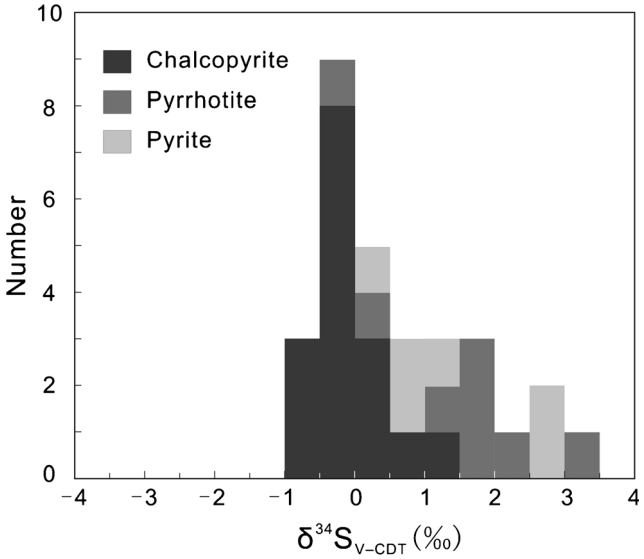

Fig. 11 Histograms of $\delta^{34}S_{V\text{-}CDT}$ values of sulfide minerals in the Sin Quyen deposit

0.33), with pronounced positive Eu anomalies (Eu/Eu* = 2.71 to 3.06) (Fig. 8b).

U-Pb ages of zircon and monazite from ore samples

High-luminescence cores of type A zircon grains have concordant to sub-concordant ages, with $^{207}Pb/^{206}Pb$ and $^{206}Pb/^{238}U$ ages ranging from 923 to 1848 Ma and from 877 to 1791 Ma, respectively (Fig. 9a). The rims of type A grains and types B to D zircon grains give a wide range of apparent Pb/U ages but consistent $^{207}Pb/^{206}Pb$ ages (Fig. 9b). These analyses define a regression line with an upper concordia intercept at 854 ± 10 Ma (MSWD = 2.5). Such a data distribution is commonly interpreted to reflect post-crystallization Pb loss (Williams 1998), possibly due to high U concentrations (mostly >1500 ppm) in zircon. It is notable that 12 spots with relatively large discordances have scattered $^{207}Pb/^{206}Pb$ ratios, and their $^{206}Pb/^{238}U$ ratios obviously deviate from the main cluster (ESM-Table 2). Such a feature indicates that both the Pb/Pb and U/Pb systems of these spots may have been partially modified. Excluding these spots, the remaining analyses yielded an upper concordia intercept at 841 ± 12 Ma (MSWD = 2.6). We consider that this upper intercept age better represents the timing of zircon formation.

For monazite, 34 analyses were conducted on 18 grains. Ten analyses, conducted on pore-free regions, yielded concordant to sub-concordant ages (−5% < discordance < 5%), which form a coherent cluster on the concordia with a weighted mean $^{206}Pb/^{238}U$ age of 837 ± 11 Ma (MSWD = 0.97). Twenty-one analyses, conducted on either pore-free or pore-bearing regions, yielded discordant ages (discordance less than −5%), but their $^{207}Pb/^{206}Pb$ data are generally consistent with the concordant data group. Thus, these 21 analyses, together with the concordant data, define an upper concordia intercept at 836 ± 18 Ma (MSWD = 0.25) (Fig. 9c). Two analyses on pore-bearing regions (LC44–8 and LC44–9) are discordant and give obviously younger $^{207}Pb/^{206}Pb$ ages. One analysis adjacent to pore-bearing region (LC44–4) is discordant and has an older $^{207}Pb/^{206}Pb$ age, which is probably caused by the presence of older inherited components. These three analyses were disregarded for the age calculation.

U-Pb age of zircon from post-ore granitic dike

Fifteen spots were measured on 15 zircon grains from the granitic dike. Fourteen analyses yielded a concordant and coherent cluster on the concordia, with a weighted average $^{206}Pb/^{238}U$ age of 736 ± 7 Ma (MSWD = 3.4) (Fig. 9d). This age is considered as the crystallization age of the granitic dike. One analysis (SQ-80-09) is discordant on concordia and has an older $^{207}Pb/^{206}Pb$ age, which is probably caused by the existence of older inherited components.

Rb-Sr isotopic composition

The ore samples have $^{87}Rb/^{86}Sr$ and $^{87}Sr/^{86}Sr$ ranging from 0.142 to 26.1 and from 0.716959 to 0.739216, respectively. Compared with ore, biotite separates have much higher $^{87}Rb/^{86}Sr$ (162 to 508) and $^{87}Sr/^{86}Sr$ (0.784105 to 0.942858) ratios. In the plot of $^{87}Rb/^{86}Sr$ vs. $^{87}Sr/^{86}Sr$, the ore samples and biotite lie along a reference line for 30 Ma (Fig. 10).

Sulfur isotope composition

The sulfide minerals have $\delta^{34}S_{V\text{-}CDT}$ values ranging from −0.8 to 3.1 (Fig. 11). Pyrite and pyrrhotite have similar $\delta^{34}S_{V\text{-}CDT}$ values, which range from 0.5 to 2.7 and from −0.1 to 3.1, respectively. These values are slightly higher than those of chalcopyrite (−0.8 to 1.3).

Discussion

Hydrothermal origin of zircon and monazite from ore samples

High-luminescence cores in type A zircon have oscillatory zoning and high Th/U ratios (mostly >0.6), indicative of a magmatic origin (Hoskin and Schaltegger 2003). These cores have a wide range of U-Pb ages that are

obviously older than those of the rims and other types of zircon. Thus, these cores are likely detrital in origin, representing detrital zircon grains in ore-hosting metasedimentary rocks, i.e., the deposition of the ore-hosting rocks must have occurred after 920 Ma.

The other zircon domains are in contact with, and/or contain inclusions of garnet, allanite, or hedenbergite (Fig. 6a–c, g), indicating that zircon was formed together with these minerals. Upper amphibolite to granulite facies metamorphism can lead to the formation of zircon and skarn-like mineral assemblage (garnet + pyroxene). However, metamorphic zircon grains with ages of ~840 Ma were not found in the ore-hosting meta-sedimentary rocks of the Sin Quyen Formation (unpublished data; J.H. Yu, written communication, 2015). To a larger extent, high-grade metamorphism at Neoproterozoic has not been recognized in the Phan Si Pan belt. Therefore, a metamorphic origin for zircon and skarn-like minerals is not favored.

We note that some zircon crystals contain primary fluid inclusions. Moreover, under CL imaging, many grains display irregular zonation, a common feature of zircon formed in hydrothermal environments (Pettke et al. 2005; Lichtervelde et al. 2009). Thus, zircon was most likely formed during hydrothermal metasomatic processes. The compositions of zircon crystals are also supportive of their hydrothermal origin. For example, the analyzed crystals have remarkably low concentrations of REE, especially LREE (Fig. 8a). The probable explanation is that they were formed together with allanite and garnet, which are particularly rich in LREE and HREE, respectively (Fig. 8b). It is also notable that zircon has very high concentrations of U relative to Th, resulting in very low Th/U ratios. Such Th-poor hydrothermal zircon is not common. On the basis of the common occurrence of U-rich minerals in the deposit, it is proposed that zircon was precipitated from U-rich fluids. The concentration of Th in hydrothermal fluids is difficult to determine, but we note that zircon formed during the same stage with allanite and monazite (stage II), both of which host abundant Th (Fig. 8c). Thus, the Th-depleted nature may be largely due to coprecipitation of zircon with Th-rich monazite and allanite. Zircon grains from Sin Quyen have high $\delta^{18}O_{V\text{-}SMOW}$ values (11.9 to 14.0‰) relative to typical magmatic zircon (commonly <11‰; Valley et al. 2005). It is known that hydrothermal fluids, such as magmatic water modified through fluid/wallrock interaction, may be rich in heavier oxygen isotopes (Wang and Williams 2001; Li et al. 2015). Due to the small oxygen fractionation factors between zircon and water ($\Delta_{water\text{-}zircon}$ < 3‰ at temperatures <600 °C; Zheng 1993), it is expected that zircon precipitated from those fluids will inherit the heavier oxygen isotopic signatures. Thus, the high $\delta^{18}O_{V\text{-}SMOW}$ values of zircon imply precipitation from ^{18}O-rich hydrothermal fluids.

Formation of hydrothermal zircon in Fe oxide-(Cu-Au) systems has been rarely documented in the literature (Valley et al. 2009; Conor et al. 2010), and Zr is generally assumed to be immobile in hydrothermal fluids. However, there is evidence that mobility of Zr can be enhanced in the presence of F-rich fluids (Rubin et al. 1989, 1993; Deng et al. 2015). For example, Rubin et al. (1989) described hydrothermal zircon "stringers" in a hydrothermal fluorite deposit formed when F-rich magmatic fluids infiltrated limestone. Experimental studies also demonstrated that Zr can be efficiently transported via hydroxyfluoride complexes in hydrothermal fluids (Migdisov et al. 2011). In the Sin Quyen deposit, the presence of F-bearing minerals, such as fluorapatite and bastnaesite, indicates that the hydrothermal fluids were likely F-bearing. In fact, F-bearing fluids are also effective mediums aiding transportation and mobility of Nb and Ti (Rapp et al. 2010; Timofeev et al. 2015). As such, Zr and other elements commonly assumed immobile are locally enriched in the Sin Quyen deposit.

Although the presence of detrital monazite in the ore-hosting sedimentary rocks cannot be completely ruled out, none were found during our observations. We thus consider that abundant monazite crystals in the studied sample are unlikely to have been inherited from precursor rocks. Rather, the close association of monazite and other hydrothermal minerals (allanite and magnetite) indicates that they were precipitated from hydrothermal fluids. The low Th content (<2700 ppm) of monazite is also consistent with a hydrothermal origin (Schandl and Gorton 2004). It is noteworthy that monazite contains many pores in some portions of the grains. These portions are unlikely to be primary growth zones, as they are generally irregularly distributed (Fig. 7). Instead, they may represent hydrothermally altered domains that were formed by a dissolution-reprecipitation mechanism (Putnis 2002). The pore-bearing domains have trace element abundances different from the pore-free domains, and the U-Pb analyses on or adjacent to the pore-bearing domains always yielded discordant ages (ESM-Table 5), indicating that the alteration has led to variable degrees of trace element mobilization and Pb loss.

Geochronological constraints on the Sin Quyen deposit

Microtextural relationships show that hydrothermal zircon formed in the same stage as allanite and magnetite, such that its U-Pb age (841 ± 12 Ma) can be taken to represent

the timing of Fe and REE mineralization. This age is indistinguishable from the U-Pb age of monazite (836 ± 18 Ma), representing the timing of REE mineralization. Thus, it is proposed that the Fe and REE mineralization occurred at ~840 Ma. The timing of the Cu-Au mineralization is not directly determined in this study. However, it is notable that the Cu-Au mineralization is largely confined to the Fe-REE mineralization zones, and sulfide minerals and magnetite show the same deformation structures in banded ores. These observations indicate that the introduction of Cu-Au and Fe-REE was most likely within a single hydrothermal process, although the Cu-sulfides are paragenetically later than magnetite and allanite. It cannot be completely precluded that there were separated Fe-REE and Cu-Au mineralization events at Sin Quyen, although this is not favored by current observations. In this case, our zircon and monazite dates provide a maximum age of Cu-Au mineralization. The minimum age of Cu-Au mineralization would be ~740 Ma, the age of the granitic dike that crosscuts the Cu-Au ore.

In the plot of $^{87}Rb/^{86}Sr$ vs. $^{87}Sr/^{86}Sr$, the compositions of ore samples and biotite generally lie along a much younger reference line (30 Ma). This age is consistent with the Cenozoic activation of the ASRR shear zone (Cao et al. 2011; Liu et al. 2013). Thus, the primary Rb-Sr isotopic systems were modified by deformation and recrystallization during a Cenozoic tectonothermal event. In contrast, zircon and monazite were largely resistant to the post-ore modification, and thereby can be used to date the primary mineralization in the Sin Quyen deposit.

Implications for the ore genesis

The genesis of the Sin Quyen deposit has long been a debated issue. Ta et al. (1975) proposed that the mineralization may be related to magmatic-hydrothermal fluids derived from granitic magmas, but the age of the granitic magmatism was not known. Ishihara et al. (2011) proposed that the mineralization may be genetically related to the Cenozoic alkaline granitic magmatism. It has also been suggested that the Sin Quyen deposit is a VMS-type deposit formed coevally with mafic volcanic rocks (Gas'kov et al. 2012). Our new age for mineralization, in combination with the alteration mineralogy and S isotopic data, places new constraints on the deposit genesis.

The Sin Quyen deposit contains extensive pre-ore albite alteration. Experimental studies demonstrated that, for a fixed fluid composition, albite formation is favored by increasing temperatures (Lagache and Weisbrod 1977). Indeed, the early-stage albite alteration is usually documented to be a high-temperature (>500 °C) metasomatic process in the deeper portions of IOCG systems (Oliver et al. 2004; Xavier et al. 2012) and porphyry copper systems (Dilles and Einaudi 1992; Sillitoe 2010). The local skarn mineral assemblages are also documented in many other IOCG deposits and are commonly thought to reflect the interaction between high-temperature fluids and Ca-rich country rocks (Wang and Williams 2001; Ismail et al. 2014). Sulfide minerals from ores have a narrow range of $\delta^{34}S_{V\text{-}CDT}$ values near 0‰ (−2.5 to +1.3‰), consistent with a magmatic origin for the sulfur (Seal 2006). Assuming that the Fe-REE and Cu-Au ores formed during a single hydrothermal process, the magmatic-like sulfur isotopic composition, together with the high-temperature alteration assemblages, is indicative of a magmatic origin for the ore-forming fluids. At a temperature of 500 °C (a common temperature for the formation of garnet-rich skarn; Meinert et al. 2005), the $\delta^{18}O$ values of fluids in equilibrium with zircon vary from +14.8 to +16.9‰ (ESM-Table 4), which fall outside the range of values for magmatic water as defined by Taylor (1974). Sedimentary rocks in the upper crust, such as limestone, sandstone, and shale, tend to be enriched in the heavy oxygen isotope ($\delta^{18}O$ = +15 to +35) (Taylor 1974), so the high $\delta^{18}O$ values of fluids may be caused by fluid-wallrock interaction.

Because Neoproterozoic (740 to 860 Ma) igneous rocks are widespread in the region, it is inferred that the Neoproterozoic igneous activity likely provided heat, part of the ore-forming fluids and, by inference, metals for the orebodies. Although there are no genetically associated intrusions exposed in the mining district, it is possible that there are some hidden plutons beneath the deposit. The Sin Quyen deposit has a metal association similar to that of the Olympic Dam deposit (Cu-Au-U ± REE) in South Australia, where unexposed mafic igneous intrusions were also suggested to be important sources for the metals either directly via magmatic hydrothermal fluids or indirectly via leaching of the igneous rocks (Johnson and McCulloch 1995; Skirrow et al. 2007). We speculate that the deeply-sourced, high-temperature, magmatic-hydrothermal fluids may have been channelized by fractures in Sin Quyen and led to the formation of Fe-REE-Cu-Au replacement orebodies and associated metasomatites.

Conclusions

1. The Sin Quyen deposit contains hydrothermal zircon and monazite. Hydrothermal zircon and monazite have

indistinguishable U-Pb ages of 841 ± 12 and 836 ± 18 Ma, respectively, representing the timing of Fe-REE mineralization.
2. The hydrothermal process responsible for Fe-REE mineralization may have also precipitated the paragenetically later Cu and Au. Even if the introduction of Cu and Au was in a separated hydrothermal process, it was no later than 736 ± 7 Ma.
3. The composition of bulk-ore and biotite separates aligned along a reference Rb-Sr isochron of 30 Ma indicates that the Rb-Sr isotopic system has been modified during a post-ore metamorphic event.
4. The mineralization, at least the Fe-REE mineralization, may have a close genetic linkage with the Neoproterozoic igneous activity.

Acknowledgements We would like to express our thanks to Mr. Wen Zhao and Prof. Jinhai Yu for their help during the field work. Great thanks are extended to Prof. Julian Pearce and Dr. Jingyuan Chen for their help with the preparation of this paper. Prof. Fernando Corfu is greatly appreciated for his suggestions which substantially improve an early version of this paper. Dr. Martin Smith, Dr. Lin Hou, and an anonymous reviewer are greatly appreciated for their constructive reviews. Prof. Rolf Römer and Prof. G. Beaudoin are gratefully acknowledged for their editorial handling. This study was supported by Key Research Program of Frontier Sciences, CAS (QYZDB-SSW-DQC008), and NSFC grants (41472068, 41673048). MyDung Tran acknowledges support from Vietnam National Foundation for Science and Technology Development (105.01-2012.06).

References

Aleinikoff JN, Schenck WS, Plank MO, Srogi L, Fanning CM, Kamo SL, Bosbyshell H (2006) Deciphering igneous and metamorphic events in high-grade rocks of the Wilmington complex, Delaware: morphology, cathodoluminescence and backscattered electron zoning, and SHRIMP U–Pb geochronology of zircon and monazite. Geol Soc am Bull 118:39–64

Bao ZW, Sun WD, Li CJ, Zhao ZH (2014) U–Pb dating of hydrothermal zircon from the Dongping gold deposit in North China: constraints on the mineralization processes. Ore Geol rev 61:107–119

Black LP, Kamo SL, Allen CM, Davis DW, Aleinikoff JN, Valley JW, Mundil R, Campbel IH, Korsch RJ, Williams IS, Foudoulis C (2004) Improved $^{206}Pb/^{238}U$ microprobe geochronology by the monitoring of a trace-element-related matrix effect; SHRIMP, ID-TIMS, ELA-ICP-MS and oxygen isotope documentation for a series of zircon standards. Chem Geol 205:115–140

Bui PM (2005) Kim Binh-Lao Cai 1:200,000 geological and mineral resources map of Vietnam. Vietnam, Geological Survey of

Cai YF, Wang YJ, Cawood PA, Fan WM, Liu HC, Xing XW, Zhang YZ (2014) Neoproterozoic subduction along the Ailaoshan zone, South China: geochronological and geochemical evidence from amphibolites. Precambrian res 245:13–28

Cai YF, Wang YJ, Cawood PA, Zhang YZ, Zhang AM (2015) Neoproterozoic crustal growth of the Southern Yangtze Block: geochemical and zircon U–Pb geochronological and Lu-Hf isotopic evidence of Neoproterozoic diorit from the Ailaoshan zone. Precambrian res 266:137–149

Cao SY, Liu JL, Leiss B, Neubauer F, Genser J, Zhao CQ (2011) Oligo-Miocene shearing along the Ailao Shan-Red River shear zone: constraints from structural analysis and zircon U/Pb geochronology of magmatic rocks in the Diancang Shan massif, SE Tibet, China. Gondwana res 19:975–993

Chen HY, Clark AH, Kyser TK, Ullrich TD, Baxter R, Chen YM, Moody TC (2010) Evolution of the giant Marcona-Mina Justa iron oxide copper gold district, south-central Perú. Econ Geol 105:155–185

Chiaradia M, Schaltegger U, Spikings R, Wotzlaw JF, Ovtcharova M (2013) How accurately can we date the duration of magmatic-hydrothermal events in porphyry systems?—an invited paper. Econ Geol 108:565–584

Chu ZY, Wu FY, Walker RJ, Rudnick RL, Pitcher L, Puchtel IS, Yang YH, Wilde SA (2009) Temporal evolution of the lithospheric mantle beneath the eastern North China Craton. J Petrol 50:1857–1898

Ciobanu CL, Wade BP, Cook NJ, Mumm AS, Giles D (2013) Uranium-bearing hematite from the Olympic Dam Cu–U–Au deposit, South Australia: a geochemical tracer and reconnaissance Pb-Pb geochronometer. Lithos 238:129–147

Conor C, Raymond OL, Baker T, Lowe G (2010) Alteration and mineralisation in the Moonta-Wallaroo Mining Field Region, Olympic Domain, South Australia. In: Porter TM (ed) Hydrothermal iron oxide Cu-Au and related deposits: a global perspective, vol 3. PGC Publishing, Adelaide, pp 147–170

Deng XD, Li JW, Wen G (2015) U-Pb geochronology of hydrothermal zircons from the early Cretaceous iron skarn deposits in the Handan-Xingtai district, North China Craton. Econ Geol 110:2159–2180

Dilles JH, Einaudi MT (1992) Wall-rock alteration and hydrothermal flow paths about the Ann-Mason porphyry copper deposit, Nevada—a 6 km vertical reconstruction. Econ Geol 87:1963–2001

Duncan R, Stein H, Evans K, Hitzman M, Nelson E, Kirwin D (2011) A new geochronological framework for mineralization and alteration in the Selwyn-Mount Dore corridor, Eastern fold belt, Mt. Isa inlier, Australia: genetic implications for iron oxide-copper-gold deposits. Econ Geol 106:169–192

Gas'kov IV, Anh TT, Hoa TT, Dung PT, Nevol'ko PA, Can PN (2012) The Sin Quyen Cu-Fe-Au-REE deposit (northern Vietnam): composition and formation conditions. Russ Geol Geophys 53:442–456

Gilbert SE, Danyushevsky LV, Rodermann T, Shimizu A, Gurenko A, Meffre S, Thomas H, Large RR, Death D (2014) Optimisation of laser parameters for the analysis of sulphur isotopes in sulphide minerals by laser ablation ICP-MS. J Anal At Spectrom 29:1042–1051

Hoskin PWO, Schaltegger U (2003) The composition of zircon and igneous and metamorphic petrogenesis. Rev Mineral Geochem 53: 27–55

Hoskin PWO (2005) Trace-element composition of hydrothermal zircon and the alteration of Hadean zircon from the Jack Hills, Australia. Geochim Cosmochim Acta 69:637–648

Ishihara S, Hirano H, Hoshino M, Can PN, Dung PH, Tran TA (2011) Mineralogical and chemical characteristics of the allanite-rich copper and iron ores from the Sin Quyen mine, northern Vietnam. Bull Geol Surv Jpn 62:197–209

Ismail R, Ciobanu CL, Cook NJ, Teale GS, Giles D, Mumm AS, Wade B (2014) Rare earths and other trace elements in minerals from skarn assemblages, Hillside iron oxide–copper–gold deposit, Yorke Peninsula, South Australia. Lithos 184-187:456–477

Jackson SE, Pearson NJ, Griffin WL, Belousova EA (2004) The application of laser ablation-inductively coupled plasma-mass spectrometry to in situ U–Pb zircon geochronology. Chem Geol 211:47–69

Jagodzinski EA (2014) The age of magmatic and hydrothermal zircon at Olympic Dam. https://www.researchgate.net/publication/

271387404_The_age_of_magmatic_and_hydrothermal_zircon_at_Olympic_Dam

Johnson JP, McCulloch MT (1995) Sources of mineralizing fluids for the Olympic Dam deposit (South Australia): Sm-Nd isotope constraints. Chem Geol 121:177–199

Lagache M, Weisbrod A (1977) The system: two alkali feldspars-KCl-NaCl-H_2O at moderate to high temperatures and low pressures. Contrib Mineral Petrol 62:77–101

Leloup PH, Lacassin R, Tapponnier P, Schärer U, Zhong D, Liu X, Zhang L, Ji S, Trinh P (1995) The Ailaoshan-Red River shear zone (Yunnan, china), tertiary transform boundary of Indochina. Tectonophysics 252:3–84

Li XC, Zhao XF, Zhou MF, Chen WT, Chu ZY (2015) Fluid inclusion and isotopic constraints on the origin of the Paleoproterozoic Yinachang Fe-Cu-(REE) deposit, Southwest China. Econ Geol 110:1339–1369

Li XC, Zhao JH, Zhou MF, Gao JF, Sun WH, Tran MD (2017) Neoproterozoic granitoids from the Phan Si Pan belt, Northwest Vietnam: implication for the tectonic linkage between Northwest Vietnam and the Yangtze Block. Precambrian res **in press**

Li XH, Liu Y, Li QL, Guo CH, Chamberlain KR (2009) Precise determination of Phanerozoic zircon Pb/Pb age by multi-collector SIMS without external standardization. Geochem Geophys Geosyst 10: 1–21

Li XH, Li WX, Li QL, Wang XC, Liu Y, Yang YH (2010) Petrogenesis and tectonic significance of the ~850 Ma Gangbian alkaline complex in South China: evidence from in-situ zircon U-Pb and Hf-O isotopes and whole-rock geochemistry. Lithos 114:1–15

Li XH, Tang GQ, Gong B, Yang YH, Hou KJ, Hu ZC, Li QL, Liu Y, Li WX (2013) Qinghu zircon: a working reference for microbeam analysis of U-Pb age and Hf and O isotopes. Chin Sci Bull 58: 4647–4654

Lichtervelde MV, Melcher F, Wirth R (2009) Magmatic vs. hydrothermal origins for zircon associated with tantalum mineralization in the Tanco pegmatite, Manitoba, Canada. Am Mineral 94:439–450

Liu FL, Wang F, Liu PH, Liu CH (2013) Multiple metamorphic events revealed by zircons from the Diancang Shan-Ailao Shan metamorphic complex, southeastern Tibetan Plateau. Gondwana res 24:429–450

Liu JL, Wang AJ, Cao SY, Zou YX, Tang Y, Chen Y (2008b) Geochronology andtectonic implication of migmatites from Diancangshan, western Yunnan, China. Acta Petrol sin 24:413–420 (in Chinese with English abstract)

Liu YS, Hu ZC, Gao S, Günther D, Xu J, Gao CG, Chen HH (2008a) In situ analysis of major and trace elements of anhydrous minerals by LA-ICP-MS without applying an internal standard. Chem Geol 257: 34–43

Liu ZC, Wu FY, Yang YH, Yang JH, Wilde SA (2012) Neodymium isotopic compositions of the standard monazites used in U-Th-Pb geochronology. Chem Geol 334:221–239

Ludwig KR (2001) Users manual for Isoplot/ex rev. 2.49, spec. Publ. 1a. Berkeley Geochronology Center, Berkeley, California

Mclean RN (2001) The Sin Quyen iron oxide-copper-gold-rare earth oxide mineralization of North Vietnam, in Porter, T.M., e.d., Hydrothermal iron oxide copper–gold & related deposits: a global perspective, vol volume 2. PGC Publishing, Adelaide, pp 293–301

Meinert LD, Dipple GM, Nicolescu S (2005) World skarn deposits. Economic Geology 100th Anniversary Volume:299–336

Migdisov AA, Williams-Jones A, Van Hinsberg V, Salvi S (2011) An experimental study of the solubility of baddeleyite (ZrO_2) in fluoridebearing solutions at elevated temperature. Geochim Cosmochim Acta 75:7426–7434

Moreto CPN, Monteiro LVS, Xavier RP, Creaser RA, DuFrane A, Melo GHC, Silva MAD, Tassinari CCG, Sato K (2015a) Timing of multiple hydrothermal events in the iron oxide-copper-gold deposits of the southern copper belt, Carajás province, Brazil. Mineral Deposita 50:517–546

Moreto CPN, Monteiro LVS, Xavier RP, Creaser RA, Dufrane SA, Tassinari CCG, Sato K, Kemp AIS, Amaral WS (2015b) Neoarchean and Paleoproterozoic iron oxide-copper-gold events at the Sossego deposit, Carajás Province, Brazil: re-Os and U-Pb geochronological evidence. Econ Geol 110:809–835

Oliver NHS, Cleverley JS, Mark G, Pollard PJ, Fu B, Marshall LJ, Rubenach MJ, Williams PJ, Baker T (2004) Modeling the role of sodic alteration in the genesis of iron oxide-copper-gold deposits, eastern Mount Isa block, Australia. Econ Geol 99:1145–1176

Pelleter E, Cheilletz A, Gasquet D, Mouttaqi A, Annich M, El Hakour A, Deloule E, Féraud G (2007) Hydrothermal zircons: a tool for ion microprobe U-Pb dating of gold mineralization (Tamlalt-Menhouhou gold deposit-Morocco). Chem Geol 245:135–161

Pettke T, Audetat A, Schaltegger U, Heinrich CA (2005) Magmatic-tohydrothermal crystallization in the W-Sn mineralized mole granite (NSW, Australia)-part II: evolving zircon and thorite trace element chemistry. Chem Geol 220:191–213

Pham QD (2015a) Exploration report on no.3 and no.7 orebodies of the Sin Quyen copper deposit, Lao Cai Province (in Vietnamese)

Pham TH, Chen FK, Wang W, Nguyen TBT, Bui MT, Nguyen QL (2009) Zircon U-Pb ages and Hf isotopic composition of the Posen granite in northwest Vietnam. Acta Petrol Sin 25:3141–3152

Pham TH (2010) Crustal Evolution and Tectonic Provenance of the Basement in the Phan Si Pan area, Northwestern Vietnam. Dissertation, Graduate School, Chinese Academy of Science

Pham TH (2015b) The Ngoi Chi Formation in the Phan Si Pan area of Northwest Vietnam revealed by zircon U-Pb age and Hf isotope composition. Acta Geosci sin 36:755–760

Putnis A (2002) Mineral replacement reactions: from macroscopic observations to microscopic mechanisms. Mineral mag 66:689–708

Qi XX, Zeng LS, Zhu LH, Hu ZC, Hou KJ (2012) Zircon U-Pb and Lu-Hf isotopic systematics of the Daping plutonic rocks: implications for the Neoproterozoic tectonic evolution of the northeastern margin of the Indochina block, Southwest China. Gondwana res 21:180–193

Qi XX, Santosh M, Zhu LH, Zhao YH, Hu ZC, Zhang C, Ji FB (2014) Mid-Neoproterozoic arc magmatism in the northeastern margin of the Indochina block, SW China: Geochronological and petrogenetic constraints and implications for Gondwana assembly. Precambrian Res 245:207–224

Rapp JF, Klemme S, Butler IB, Harley SL (2010) Extremely high solubility of rutile in chloride and fluoride-bearing metamorphic fluids: an experimental investigation. Geology 38:323–326

Rimsa A, Whitehouse MJ, Johansson L, Piazolo S (2007) Brittle fracturing and fracture healing of zircon: an integrated cathodoluminescence, EBSD, U–Th–Pb, and REE study. Am Mineral 92:1213–1224

Rubin JN, Henry CD, Price JG (1989) Hydrothermal zircons and zircon overgrowths, Sierra Blanca Peaks, Texas. Am Mineral 74:865–869

Rubin JN, Henry CD, Price JG (1993) The mobility of zirconium and other immobile elements during hydrothermal alteration. Chem Geol 110:29–47

Schaltegger U (2007) Zircon tiny but timely: hydrothermal zircon. Elements 3:51–79

Schandl ES, Gorton MP (2004) A textural and geochemical guide to the identification of hydrothermal monazite: criteria for selection for samples for dating epigenetic hydrothermal ore deposits. Econ Geol 99:1027–1035

Seal RR (2006) Sulfur isotope geochemistry of sulfide minerals. Rev Mineral Geochem 61:633–677

Sillitoe RH (2010) Porphyry copper systems. Econ Geol 105:3–41

Skirrow RG, Bastrakov EN, Barovich K, Fraser GL, Creaser R, Fanning MC, Raymond OL, Davidson GJ (2007) Timing of iron oxide Cu-Au-(U) hydrothermal activity and Nd isotope constraints on metal sources in the Gawler craton, South Australia. Econ Geol 102:1441–1470

Stacey JS, Kramers JD (1975) Approximation of terrestrial lead isotope evolution by a two-stage model. Earth Planet Sci Lett 26:207–221

Ta VD et al (1975) The geological report on detailed exploration of the Sin Quyen copper deposit. General Department of Geology, Hanoi (unpublished).

Tapponnier P, Lacassin R, Leloup PH, Scharer U, Zhong D, Wu HH, Liu X, Ji S, Zhang L, Zhong J (1990) The Ailao Shan–Red River metamorphic belt: tertiary left-lateral shear between Sundaland and South China. Nature 343:431–437

Taylor HP Jr (1974) The application of oxygen and hydrogen isotope studies to problems of hydrothermal alteration and ore deposition. Econ Geol 69:843–883

Tran TT (2011a) Meso-Neoarchean Supersequence. In: Nguyen KS (ed) Geology and earth resources of Vietnam. Publishing House for Science and Technology, Hanoi, p 37

Tran TT (2011b) Paleoproterozoic-Middle Neoproterozoic Supersequence. In: Nguyen KS (ed) Geology and earth resources of Vietnam. Publishing House for Science and Technology, Hanoi, p 37

Timofeev A, Migdisov AA, Williams-Jones AE (2015) An experimental study of the solubility and speciation of niobium in fluoride-bearing aqueous solutions at elevated temperature. Geochim Cosmochim Acta 158:103–111

Trotter JA, Williams IS, Barnes CR, Lécuyer C, Nicoll RS (2008) Did cooling oceans trigger Ordovician biodiversification? Evidence from conodont thermometry. Science 321:550–554

Usuki T, Lan CY, Tran TH, Phan TD, Wang KL, Shellnutt GJ, Chung SL (2015) Zircon U–Pb ages and Hf isotopic compositions of alkaline silicic magmatic rocks in the Phan Si Pan-Tu Le region, northern Vietnam: identification of a displaced western extension of the Emeishan Large Igneous Province. J Asian Earth Sci 97:102–124

Valley PM, Hanchar JM, Whitehouse MJ (2009) Direct dating of Fe-oxide (–Cu–Au) mineralization by U–Pb zircon geochronology. Geology 37:223–226

Valley PM, Fisher CM, Hanchar JM, Lam R, Tubrett M (2010) Hafnium isotopes in zircon: a tracer of fluid-rock interaction during magnetite–apatite ("Kiruna-type") mineralization. Chem Geol 275:208–220

Valley JW, Lackey JS, Cavosie AJ, Clechenko CC, Spicuzza MJ, Basei MAS, Bindeman IN, Ferreira VP, Sial AN, King EM, Peck WH, Sinha AK, Wei CS (2005) 4.4 billion years of crustal maturation: oxygen isotopes in magmatic zircon. Contribution to Mineralogy and Petrology 150:561–580

Wang SQ, Williams PJ (2001) Geochemistry and origin of Proterozoic skarns at the Mount Elliott Cu-Au(-Co-Ni) deposit, Cloncurry district, NW Queensland, Australia. Mineral Deposita 36:109–124

Wang W, Cawood PA, Zhou MF, Zhao JH (2016) Paleoproterozoic magmatic and metamorphic events link Yangtze to northwest Laurentia in the Nuna supercontinent. Earth Planet Sci Lett 433:269–279

Williams IS (1998) U-Th-Pb geochronology by ion microprobe. Rev Econ Geol 7:1–35

Xavier RP, Monteiro LVS, Moreto CPN, Pestilho ALS, Melo GHC, Silva MAD, Aires B, Ribeiro C, Freitas e Silva FH (2012) The iron oxide copper-gold systems of the Carajás mineral province, Brazil. Society of Economic Geologists Special Publication 16:433–453

Zhao XF, Zhou MF, Li JW, Selby D, Li XH, Qi L (2013) Sulfide Re-Os and Rb-Sr isotopic dating of the Kangdian IOCG metallogenic province, SW China: implications for regional metallogenesis. Econ Geol 108:1489–1498

Zheng YF (1993) Calculation of oxygen isotope fractionation in anhydrous silicate minerals. Geochim Cosmochim Acta 57:1079–1091

Zhou MF, Zhao XF, Chen WT, Li XC, Wang W, Yan DP, Qiu HN (2014) Proterozoic Fe-Cu metallogeny and supercontinental cycles of the southwestern Yangtze block, southern China and northern Vietnam. Earth-Sci rev 139:59–82

Zhou Q, Jiang YH, Zhao P, Liao SY, Jin GD, Liu Z, Jia RY (2012) SHRIMP U-Pb dating on hydrothermal zircons: evidence for an Early Cretaceous epithermal event in the Middle Jurassic Dexing porphyry copper deposit, Southeast China. Econ Geol 107:1507–1514